ADVANCED ELECTRONIC MATERIALS Open Access
www.advelectronicmat.de

Enhanced Coupling Between Soft Ferromagnetism and Displacive Ferroelectricity in the Pb-Site Modified $PbFe_{1/2}Nb_{1/2}O_3$

Ji-Hun Park, Jae-Hyeon Cho, Nyun Jong Lee, Hyun-Jae Lee, Ju-Hyeon Lee, Geon-Ju Lee, Frederick P. Marlton, Motohiro Suzuki, Manuel Hinterstein, Yoon Seok Oh, Ji-Won Choi, Geon-Tae Hwang, Jun Hee Lee, Sanghoon Kim, Kee Hoon Kim, and Wook Jo**

Albeit having great potential toward unprecedented type of applications such as magnetoelectric (ME) sensors and memories, practically useful single-phase multiferroics that show large coupling between ferromagnetism and ferroelectricity at ambient temperatures are still lacking. Here, the discovery of a new type of perovskite ferroelectrics (Pb,M)($Fe_{1/2}Nb_{1/2}$)O_3 (M = Fe, Co, Ni) is reported with a magnetically-active metal ion introduced into a cuboctahedrally-coordinated Pb position, which exhibits enhanced ME coupling owing to the development of simultaneous soft-ferromagnetism and lone-pair ferroelectricity persistent above room temperature. These Pb-site engineered (Pb,M)($Fe_{1/2}Nb_{1/2}$)O_3 perovskites exhibit a ME coupling coefficient of ≈40–60 ps m^{-1}, a saturated electric polarization of 14–17 μC cm^{-2} and a saturation magnetization of 0.15–0.3 μ_B $f.u^{-1}$. X-ray absorption spectroscopy combined with first-principles calculations demonstrates that the induced ferromagnetism originates from the ferromagnetic superexchange interaction coming from ≈90° bonding between the magnetic ions at the Pb site. The present discovery of the enhanced ME coupling in the Pb-site engineered perovskite ferroelectrics may provide unforeseen opportunities for applying conventional displacive ferroelectricity in the field of spintronics where ferromagnetism is essentially required.

1. Introduction

The realization of multiferroicity with large ME coupling (x) in single-phase homogeneous materials at ambient temperatures has garnered great interest due to its potential for novel applications.[1–9] Single-phase multiferroics can be generally classified as either Type I or II. In the Type I multiferroics, wherein largely independent (anti-)ferromagnetic and ferroelectric orders merely coexist, the cross-coupling between the magnetism and the ferroelectricity, i.e., magnetoelectric (ME) coupling (o) is rather weak. On the other hand, the Type-II multiferroics, termed often as magnetic ferroelectrics,[10] exhibit inversion symmetry breaking with a simultaneous spin ordering, which is driven by a unique spin-lattice coupling mechanism such as the inverse Dzyaloshinskii–Moriya (DM) interaction.[11–13] Although the ME coupling itself can be large in Type II multiferroics, the ferroelectric

J.-H. Park, J.-H. Cho, J.-H. Lee, G.-J. Lee, W. Jo
Department of Materials Science and Engineering
Ulsan National Institute of Science and Technology (UNIST)
Ulsan 44919, Republic of Korea
E-mail: wookjo@unist.ac.kr

J.-H. Cho
Flash TD Team
Semiconductor R&D Center
Samsung Electronics
Yongin 17113, Republic of Korea

The ORCID identification number(s) for the author(s) of this article can be found under https://doi.org/10.1002/aelm.202400370

DOI: 10.1002/aelm.202400370

N. J. Lee, S. Kim
Department of Physics
University of Ulsan
Ulsan 44610, Republic of Korea

H.-J. Lee, J. H. Lee
Department of Energy and Chemical Engineering
Ulsan National Institute of Science and Technology (UNIST)
Ulsan 44919, Republic of Korea

F. P. Marlton
Centre for Clean Energy Technology
School of Mathematical and Physical Sciences
Faculty of Science
University of Technology Sydney
Sydney, New South Wales 2007, Australia

M. Suzuki
Japan Synchrotron Radiation Research Institute
Sayo, Hyogo 679–5198, Japan

polarization modulated by spin order is often too small to be useful in practical applications. Moreover, achieving large ME coupling at room temperature remains challenging due to the relatively low spin ordering temperatures.

Numerous research on the multiferroics for practical applications at room temperatures have thus focused on the Type I multiferroics wherein displacive ferroelectricity can provide larger ferroelectric polarization than Type II. From this perspective, the discovery of the most promising Type I multiferroicity in bismuth ferrite ($BiFeO_3$, BFO), exhibiting its prominent displacive ferroelectricity along with antiferromagnetism above room temperature,[14,15] has motivated intense research on perovskite-structured ME multiferroics. However, their magnetic properties (i.e., canted ferromagnetism) or/and coupling coefficients are still weak at ambient temperature (order of a few ps m^{-1}) because of their independent origins of the ferroic orders.[16–19] Therefore, a new strategy for realizing the Type I multiferroics with large ME coupling must be developed to overcome current limits in the existing Type I multiferroics. The most plausible route toward this end is expected to naturally involve the creation of a mechanism that exhibits stronger coupling between ferromagnetism and ferroelectricity in the Type I multiferroics.

Herein, we propose a novel strategy of inducing ferromagnetism and significant ME coupling in a displacive ferroelectric perovskite, lead iron niobate ($PbFe_{1/2}Nb_{1/2}O_3$, PFN), in which magnetic ions are partially introduced into the lone pair Pb site, thus termed as magnetoelectric displacive ferroelectrics (MDFs). Generally, magnetically active transition metals, such as Fe, Co, and Ni, occupy the B site in the perovskites with the chemical formula of ABO_3 owing to their relatively small ionic sizes due to the constraint of the Goldschmidt tolerance factor, resulting in antiferromagnetic superexchange interaction close to 180°.[20–23] This is one of the reasons why perovskite oxides exhibit antiferromagnetic order in the presence of magnetic ions in their lattices. However, when a magnetic ion is introduced into the A site, a 90° bypass for the spin exchange path is created, rendering the e_g orbitals of neighboring magnetic elements become orthogonal. This leads to the ferromagnetic superexchange interaction,[24–27] as predicted by the Goodenough-Kanamori rule. Furthermore, enhanced, direct bilinear ME interaction described by a free energy term of ≈MP where M (P): ferromagnetic (ferroelectric) order parameter, can be expected. It is likely that enhanced ferromagnetic moment by more than 500 times can boost up the magneto-elastic coupling that can in turn modulate displacement for the ferroelectric polarization, resulting effectively the bilinear ME coupling term.

2. Results and Discussion

To demonstrate the feasibility of the proposed Pb-site engineering strategy, we choose a model system of PFN,[28–30] because as compared with BFO, PFN is easier to fabricate as a phase-pure bulk ceramic with satisfactory ferroelectric properties. We have substituted several magnetic ions for Pb at the A-site to prepare a series of MDFs, based on the stoichiometric formulae $(Pb_{1-x}Fe_x)(Fe_{1/2}Nb_{1/2})O_3$ (PFFN100x), $(Pb_{1-x}Co_x)(Fe_{1/2}Nb_{1/2})O_3$ (PCFN100x), and $(Pb_{1-x}Ni_x)(Fe_{1/2}Nb_{1/2})O_3$ (PNFN100x). We have found that the three sets of compositions yield similar Type I multiferroics with significant ME coupling. On the other hand, we mainly present the results on PNFN20 as a representative case in the main text while a full dataset of the others is provided in the Supporting information.

The X-ray diffraction (XRD) profile indicates that the Pb ions are successfully replaced by the Ni ions without secondary phases within the detection limit of the apparatus used (see **Figure 1a**). The decrease in the lattice constant with the Ni ion substitution constitutes a piece of evidence that the Ni ion, of which charge number of 2+ as determined through XAS analysis, is introduced into the A-site; the ionic radius of Ni^{2+} is much smaller than that of Pb^{2+}, whereas it is larger than those of Fe^{3+} and Nb^{5+}. Furthermore, the unnormalized XRD peak intensity of the pristine PFN is less than that of PNFN20. Given that the X-ray absorption coefficient of Pb ions is much larger than that of Ni ions,[31] this observation demonstrates that Pb ions are indeed substituted by Ni ions as intended. The atomic position of PNFN20 was demonstrated via the Rietveld refinement using the Fullprof program,[32] which indicated the preference of the Ni ion to sit at the corner of the cuboctahedron rather than at the center (Figure S1, Supporting Information).

The proposed Pb-site engineering strategy was also verified on PNFN20 using X-ray absorption spectroscopy (XAS), through which the ionic valance state of each cation can be determined. The XAS spectra of both PNFN20 and pristine PFN, measured at the Fe *L*-edge, are practically the same as that of α-Fe_2O_3 with a corundum structure, in which the Fe sites are located nearly at the center of a perfect octahedron with Fe^{3+} ions formally (see Figure 1b).[33] However, the spectra are quite different from that of γ-Fe_2O_3, which has the combined contribution of Fe^{3+} ions in both tetrahedral and octahedral geometry.[34] These findings indicate that Fe^{3+} ions are exclusively located at the B-sites in both pristine PFN and PNFN20, strongly suggesting that Ni ions are introduced solely into the A-sites. Furthermore, the XAS spectrum of the Ni *L*-edge closest to that of Ni^{2+} in an octahedrally coordinated environment (see Figure 1c),[35,36] while it is obviously different from those of the Ni^{3+} spectrum and of the Ni^{2+} in the pyramidal spectrum. Therefore, the Ni

M. Hinterstein
Institute for Applied Materials
Karlsruhe Institute of Technology (KIT)
Haid-und-Neu Strasse 7, 76131 Karlsruhe, Germany
Y. S. Oh
Department of Physics
Ulsan National Institute of Science and Technology (UNIST)
Ulsan 44919, Republic of Korea
J.-W. Choi
Electronic Materials Center
Korea Institute of Science and Technology (KIST)
Seoul 02792, Republic of Korea
G.-T. Hwang
Department of Materials Science and Engineering
Pukyong National University
Busan 42601, Republic of Korea
K. H. Kim
Department of Physics and Astronomy
CeNSCMR & Institute of Applied Physics
Seoul National University
Seoul 151–747, Republic of Korea
E-mail: optopia@snu.ac.kr

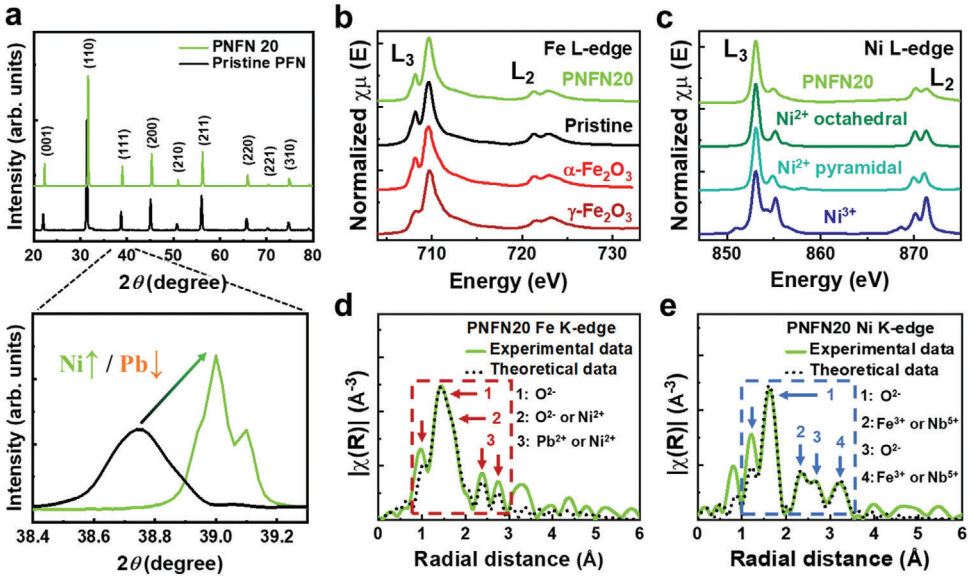

Figure 1. X-ray diffraction (XRD) and absorption spectroscopy (XAS) profiles of pristine PFN and PNFN20. a) Normalized XRD pattern reveals a well-defined single-phase perovskite structure. *I*(111) is magnified using raw data, i.e., the unnormalized intensity, to show the changes in peak position and intensity with Ni ion substitution. The XAS spectra measured at b) Fe and c) Ni L-edge along with reference spectra for comparison. The Fourier transform of the extended X-ray absorption fine structure (EXAFS) spectra superimposed with a simulation-generated profile reveals an interatomic distance for d) Fe and e) Ni K-edge. The arrows are drawn to indicate neighboring ions with the corresponding orders.

ions in PNFN20 are likely located at the A site, which has a higher atomic coordination number, with an oxidation state of 2+.

To clarify further where transition metals are located, we have also performed the extended X-ray absorption fine structure (EXAFS) of PNFN20 as shown in Figures 1d,e (the corresponding XAS spectra at the K-edge was shown in Figure S2, Supporting Information), through which the atomic configuration can be determined based on interatomic distance analysis.[37–40] The Fourier-transformed EXAFS data were combined with a simulation-generated profile to provide compelling evidence for the determination of the local environment of Fe and Ni ions. The EXAFS spectrum of Fe ions in Figure 1d reveals that the first peak relating to the nearest O ions has a shoulder in front of it, implying that the Fe was off-centered due to the O cage distortion. The simulation results also suggest that the hidden peak contributed by the scattering of O and Ni ions can be embedded in the right wing of the main peak. The next doublet, located in the range of 2–3 Å, indicates that there are two different occupied places at the A-sites centering around the Fe ions.

Given that the EXAFS spectrum of Ni ions in Figure 1e is significantly different from that of Fe ions, it is plausible that Ni ions are located at the A site rather than the B site. This is further supported by the fact that the distance between the Ni and O ions is greater than the distance between the B site and the O ions. It was revealed that both the first peak attributable to the scattering of the nearest O ion and the second peak attributable to the scattering of the ions sitting at the B-sites are well split, indicating that the Ni ions are off-centered. Considering the obtained local environment around the Fe^{3+} and Ni^{2+} ions, it is plausible that the Ni ions sit at the corners of the A-sites of the perovskite structure rather than at the B-sites. Based on the data interpretation from the EXAFS, **Figure 2a** schematically illustrates the local environment of Ni ions, in which the position of Ni ion is shifted toward a corner of the cuboctahedral A-site.

The density functional theory (DFT) calculation was employed to determine the spin configuration to account for the origin of the ferromagnetism in MDFs, based on the established atomic configuration obtained through X-ray-related analyses. The DFT calculation suggests a canting-free perovskite structure with the space group of R3m as the most stable form. However, the pristine PFN itself is known to be a canted antiferromagnet like BFO, with an oxygen octahedral tilting, thus belonging to the space group of R3c.[41] This discrepancy may arise from the fact that the cell size for the current calculation is insufficient to consider the long-wavelength period typically required for a stable canted antiferromagnetic order.[15,42] Although the effect of spin-canting cannot be reflected, the DFT calculation suggests that the soft ferromagnetism is induced by the A-site engineering (Figure 2b) through the two key mechanisms. First, the displaced Ni^{2+} ions cause two nearby oxygen octahedra to be tilted even more. Second, through an in-between oxygen ion, the Ni^{2+} spin can align ferromagnetically with the spin of the nearest Fe^{3+} ion via a 90° superexchange interaction, while that of the second nearest Fe^{3+} ion is arranged in the opposite direction. This is evidenced by the calculated superexchange parameters between Ni^{2+} and Fe^{3+} ions in PNFN20, i.e., J_{AFM} and J_{FM}, based on the pristine PFN results (Figures S4–S6, Supporting Information); the superexchange parameter between Ni and the nearest Fe ion (J_{FM}) is slightly larger than that between Ni and the next nearest Fe ion (J_{AFM})., i.e., Ni ions effectively align ferromagnetically with the nearest Fe ions while they align antiferromagnetically with the next nearest Fe ions.[43] Thus, all experimental and theoretical data indicate that the introduced Ni ion is located at the corner of the A-site, and interacts with two Fe ions located at a slightly different distance

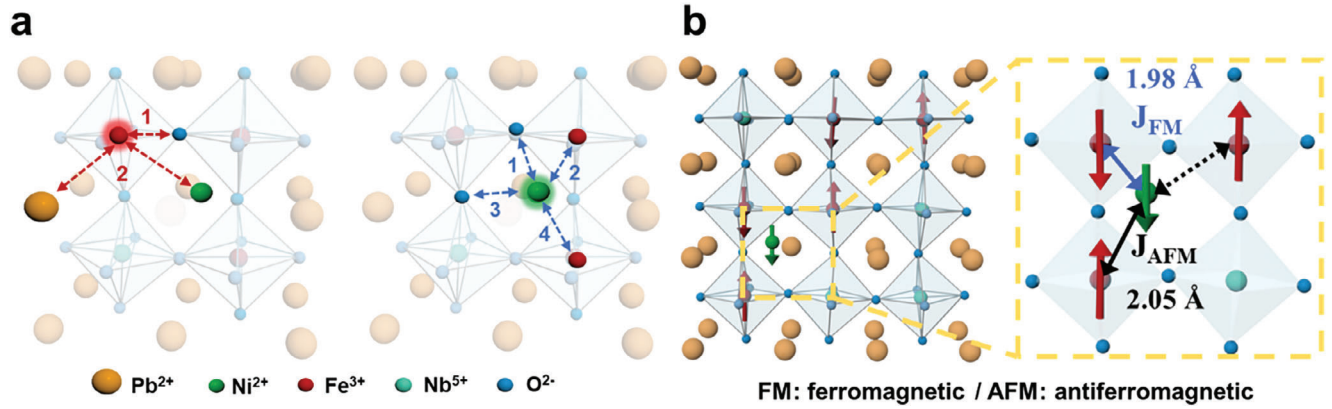

Figure 2. Schematics of a) the local environment around Fe^{3+} and Ni^{2+} ions established by the extended X-ray absorption fine structure (EXAFS) results and b) spin configuration determined by the first principle calculation. The superexchange parameter is denoted as *J* with feasible spin exchange interactions, and the arrows for the Fe (red) and Ni (green) ions represent the magnetic spin states. The degree of exchange interaction is indicated by the color and the type of arrow; a blue and solid arrow implies a stronger interaction than a black and dashed arrow, respectively.

to the Ni ion of ≈0.07 Å, coming from an oxygen octahedral tilting. The resultant interaction produces stronger ferromagnetic interaction with the nearest Fe ions.

The stability of the perovskite structure is determined by the Goldschmidt tolerance factor based on the ionic size of each element in ABO_3; a larger cation with a low valency and a smaller cation with a higher valency occupy the A-site that is surrounded by 12 oxygen ions and the B-site that is octahedrally coordinated with 6 oxygen ions, respectively. Therefore, usual magnetically active ions belonging to 3*d* transition metals are positioned at the center of the oxygen octahedral cage in the case of representative Pb- or Bi-based lone-pair ferroelectrics with the perovskite structure. This means that when the B sites are filled with magnetically active ions, the spin alignment becomes antiparallel owing to the antiferromagnetic superexchange interaction, according to the Goodenough-Kanamori rule.[25,26] As a result, the PFN system considered in this study, in which the magnetically active Fe^{3+} ions populate only the B sites, exhibits paramagnetism with a relatively small coercive field and remnant magnetization due to spin clustering,[42,44,45] as shown in **Figure 3a**. On the other hand, introducing magnetically active elements simultaneously into the A and B sites can result in a

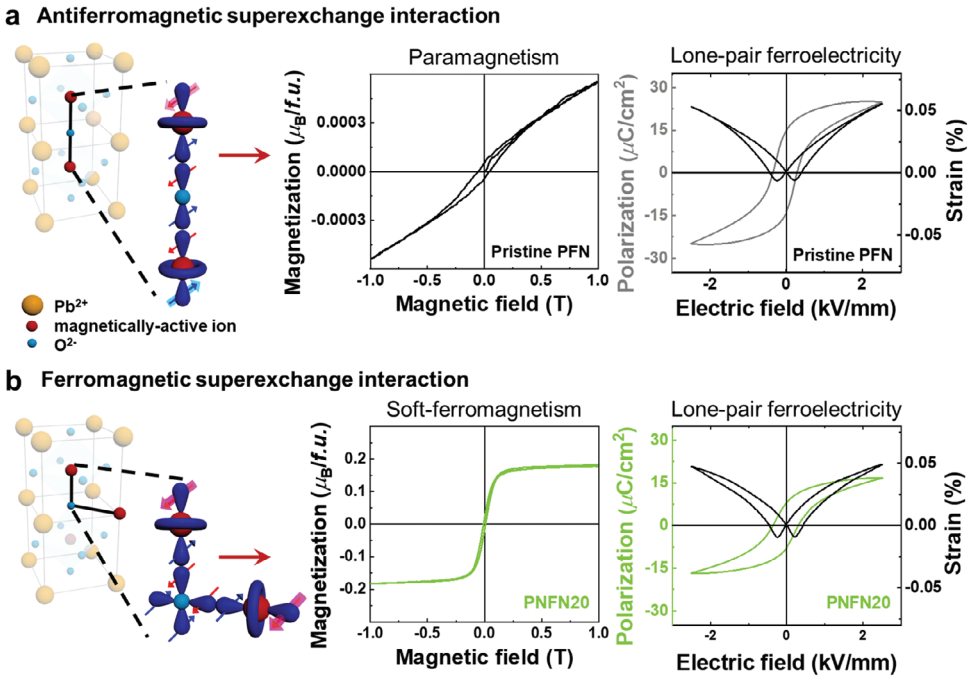

Figure 3. Schematics of both a) antiferromagnetic and b) ferromagnetic superexchange interactions along with the magnetic and ferroelectric behavior of the pristine and engineered PFN systems. The ferromagnetic superexchange interaction results in soft ferromagnetism coexisting with the existing displacive ferroelectricity, in contrast to the antiferromagnetic superexchange interaction.

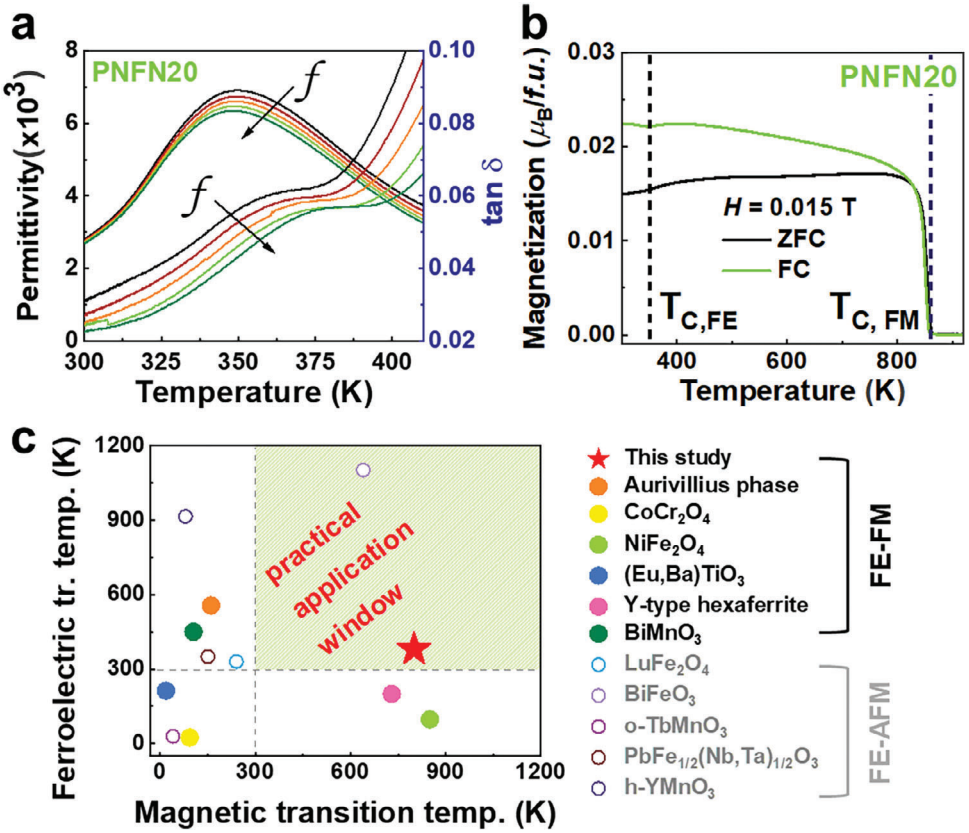

Figure 4. Transition temperatures and magnetoelectric (ME) coupling of PNFN20. a) Temperature-dependent dielectric permittivity with variable frequencies (*f*), which doubles in stages from 1 to 16 kHz along the direction of the arrow, manifests the ferroelectric Curie temperature ($T_{C,\ FE}$). b) The magnetization versus temperature (MT) plot exhibits ferromagnetic transition temperature ($T_{C,\ FM}$). c) A currently state of multiferroic oxides in terms of their transition temperatures and magnetic types, demonstrating that MDFs are the only magnetoelectrically active "Type I" multiferroics exhibiting both ferroelectricity (FE) and ferromagnetism (FM) above 300 K.

ferromagnetic superexchange interaction through the bypassing of the superexchange interaction path, as schematically illustrated in Figure 3b. It is noted that replacing Pb^{2+} ions with 20 at% Ni^{2+} ions (thus forming the PNFN20) yields soft ferromagnetism with a considerable magnetization of ≈0.2 μ_B f.u.−1, which is ≈500 times larger than that of the pristine, and a saturation magnetic field as low as ≈0.1 T. To our surprise, the PNFN20 system preserves the preexisting ferroelectricity (an intuitive demonstration of the coexistence of ferromagnetism and ferroelectricity is provided in Movie S1, Supporting Information); a saturated ferroelectric polarization was measured as ≈17 μC cm^{-2} and a butterfly shape, which is typical for normal ferroelectrics, is evident in the corresponding electromechanical strain hysteresis loop with a value of 180 pm V^{-1} at 2.5 kV mm^{-1}.

We argue that the generation of ferromagnetism in the MDFs is owing to the intended A-site engineering, as the saturation magnetization doubles when the concentration of Ni doubles from 10 to 20 at.%. The observed magnetic properties in PNFN20 do not come from the possible presence of ferromagnetically active secondary phases such as $NiFe_2O_4$ (NFO) as the NFO, if any, is well below the detection limit of the XRD profile.[46,47] Moreover, we have confirmed that the mere mixture of pure PFN and NFO with ≈5 wt.%, which produces apparently similar magnetic properties with PNFN20, resulted in ferroelectricity and ME coupling behaviors completely different from those of PNFN20. In addition, the mixture reveals the secondary phases even at 1 wt.% NFO addition (Figure S3, Supporting Information). This is clearly evidenced by a full data set, presented in Figures S7 and S8 (Supporting Information). It is noted that a small deterioration of ferroelectricity of PNFN20 as compared with that of PFN (≈22 μC cm^{-2} for saturated polarization) is also consistent with our claim, considering that the magnetically active elements replacing Pb^{2+} are ferroelectrically inactive. Alongside, the piezoelectric coefficients (d_{33}) were measured to be similar at ≈120 pC/N before and after Pb-site engineering. This indicates that replacing magnetically active elements plays a significant role in the lattice deformation during the switching process, without contributing to the polarization state. This is likely caused by the oxygen octahedra tilting as discussed above.

The temperature-dependent dielectric permittivity of PNFN20 implies that the MDFs undergo a diffuse phase transformation (**Figure** 4a; Figure S10, Supporting Information). Intriguingly, a certain dielectric relaxation occurs in the temperature range of 340–370 K, as evidenced by the frequency-dependent inflection points in the dielectric loss. This dielectric relaxation appears to be closely related to the transition between a ferroelectric and a paraelectric order. As shown in the magnetization versus

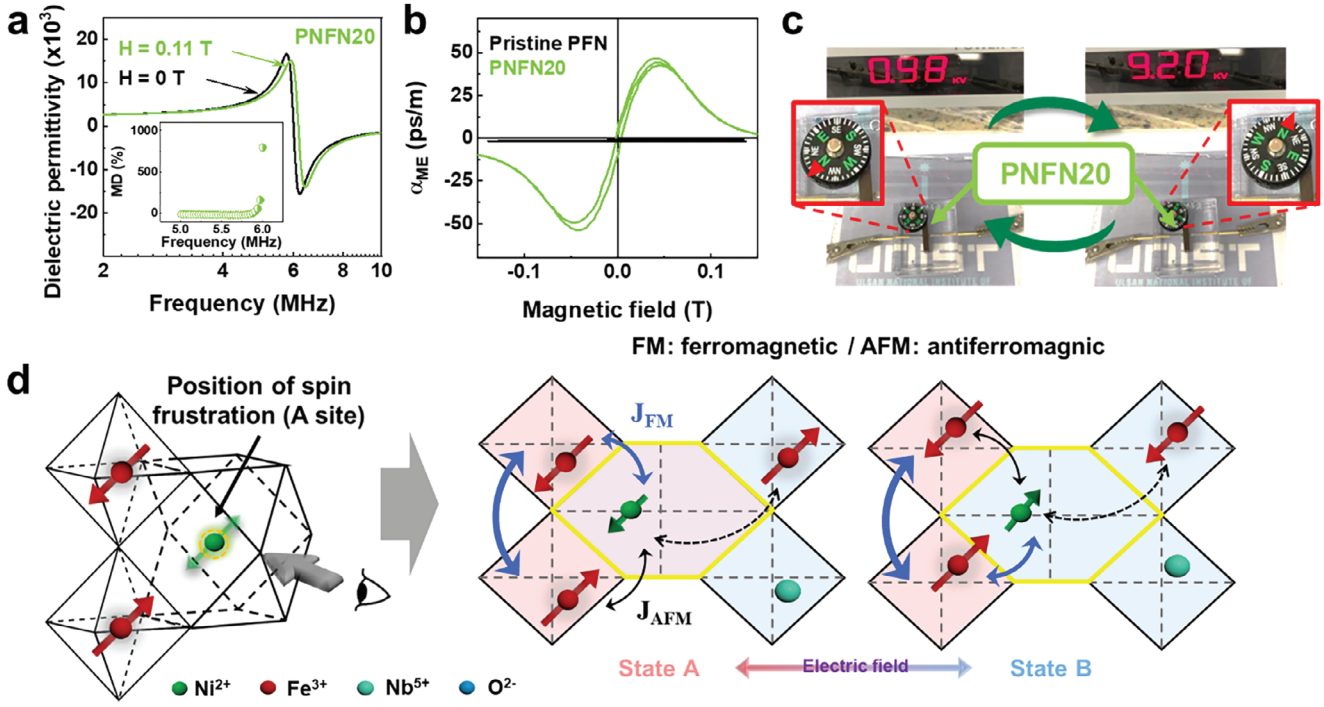

Figure 5. Magnetoelectric (ME) coupling of PNFN20 is verified through a) a magnetodielectric (MD) coupling given by the frequency-dependent dielectric permittivity under on- and off-magnetic fields, b) a direct ME coupling in terms of the ME voltage coefficient as a function of the magnetic field, and c) a converse ME coupling manifested in the deflection of a compass needle. d) A schematic is prepared to explain ME coupling behavior based on experimental and theoretical results.

temperature (MT) curve (Figure 4b; Figure S11, Supporting Information), the magnetic Curie temperature of PNFN20 (≈860 K) seems to originate from the triangular spin configuration, similar to ferrimagnetic spinel oxides.[48,49]

The significance of the developed MDFs is most evident from the status summary presented in Figure 4c (details in Table S1, Supporting Information). The MDFs are unique among ME multiferroics in that the ferromagnetism induced by Pb-site engineering on lone-pair ferroelectric oxides is significant in magnitude since it originates exclusively from the spin moment of magnetic elements in the A-site, via the 90° ferromagnetic superexchange mechanism. The multiferroicity induced from ferromagnetic oxides is usually quite weak at ambient temperature, as demonstrated in previous studies.[10,11,19] This is because the spatial inversion asymmetry required for ferroelectricity arises from an extremely small subatomic-level anisotropy, known as the inverse DM interaction.[50–53] Therefore, the MDFs can be the unique, practically viable ferromagnetic–ferroelectric magnetoelectric oxides.

Magnetodielectric (MD) coupling, which is a phenomenon indirectly showing ME coupling, was characterized based on frequency-dependent dielectric permittivity changes under an on- and off-magnetic field strength of 0.11 T (**Figure 5a**). The shift in the resonance frequency in the presence of the magnetic field resulted in a substantial dielectric tunability of ≈800% in PNFN20 at a resonance frequency of 6 MHz. The PNFN20, as shown in Figure 5b, exhibits an expected profile for the direct ME coupling between ferromagnetism and ferroelectricity for the following reasons. First, the ME coefficient (α_{ME}) increases with increasing magnetic field, culminating with the onset of saturation in the inducible magnetization at ≈0.05 T. Second, the presence of hysteresis in the ME coupling implies that ferroelectric domains are responsive to the external magnetic field. Finally, a converse ME coupling is visualized with a compass upon the application of an electric field, which indicates voltage-driven spin control. The needle of the compass is deflected by ≈160° clockwise under the influence of the voltage-driven magnetic field, as shown in Figure 5c (videos of these demonstrations are available in Movies S2 and S3, Supporting Information).

Given that the magnetic spin of PNFN20 can be switched by a smaller magnetic field than those of PFN as supported by the magnetic coercive fields presented in Figure 3, we suppose that the ME coupling originates from the Ni^{2+} spin flipping between two nearby displaced Fe^{3+} ions with opposite spin directions; this flipping could induce greater oxygen octahedral tilting or/and magnetostriction between Ni and Fe ions depending on their spin direction and interatomic distance, resulting in bilateral ME switching in the presence of electric fields, as illustrated schematically in Figure 5d. This is supported by the characteristic coupling behaviors that vary depending on the introduced transition metals, i.e., Fe, Co, and Ni, as shown in Figures S11 and S12, Supporting Information). Although this effective direct coupling between the spin exchange interaction and ionic displacement needs further verification, the results imply that the incorporation of Ni^{2+} into the A-site is the key to realizing viable magnetoelectrically coupled multiferroic perovskite oxides.

3. Conclusion

In summary, we have demonstrated that Pb-site engineering in ferroelectric perovskite oxides with magnetically active elements can yield intrinsic ferromagnetism inherited from a ferromagnetic superexchange interaction. Considerable ME coupling arises from the interaction of intentionally introduced magnetic elements at the A-site with two nearby B-site magnetically active ions (Fe ions in this study) of different distances resulting from different oxygen octahedral tilting. Because of the room-temperature magnetoelectric coupling, together with the intrinsic ferromagnetism, MDFs exhibit superior ME coupling characteristics as compared with those found in typical Type I multiferroics. The effectiveness of the proposed strategy was confirmed through spectroscopic analyses and DFT calculations. We expect that this discovery of a new class of MDFs will open up a new opportunity for applications of conventional ferroelectrics in the field of spintronics and future industries where magnetically active ferroelectrics are essentially required.

4. Experimental Section

Fabrication of Bulk Samples of Compositionally-Modified PFN Systems: The raw powders of PbO (99.9%, Sigma–Aldrich), Fe_2O_3 (99%, Sigma–Aldrich), Nb_2O_5 (99.99%, Sigma–Aldrich), NiO (99.8%, Sigma–Aldrich) and $CoCO_3$ (99.5%, Alfa–Aesar), dried at 373 K for 24 h, were used to fabricate bulk pelletized samples by a conventional solid-state sintering technique. The mixtures of powders were calcined at 950–1100 K for 2 h and sintered at 1250–1400 K for 2 h along with Pb-excess $PbZrO_3$ powder to prevent Pb evaporation.

Measurements of the Ferroelectric Properties of the Compositionally-Modified PFN Systems: A piezoelectric measurement system (aixACCT aixPES) was used to characterize the polarization and strain hysteresis loops on usual disc-shaped samples of 1 mm in thickness and 10 mm in diameter up to the electric field strength of 2.5 kV mm^{-1} at the measurement frequency of 10 Hz. The piezoelectric coefficients (d_{33}) were measured by using a d_{33} meter (YE2730A) at a frequency of 110 Hz. Temperature-dependent dielectric permittivity and loss were measured by impedance spectroscopy (HP4192A).

Confirmation of Ferromagnetism and Magnetic Curie Temperature: Magnetic hysteresis loops were measured using a vibrating sample magnetometer (VSM, VSM7300) and a physical property measurement system (PPMS, Quantum Design).

Measurement of MD and ME Coupling: Dielectric permittivity was measured by an impedance spectroscope (HP4194A) over the measurement frequency range from 100 Hz to 40 MHz at room temperature. For the dielectric measurement under a magnetic field, i.e., magnetodielectric (MD) coupling, wired disc-shaped samples were placed in the center of two platelet neodymium magnets of 40 mm × 60 mm × 15 mm in parallel with a separation distance of 60 mm. Before the magnetoelectric (ME) measurement, the compositionally modified PFN bulk samples were DC-poled at 1 kV mm^{-1} for 20 min at room temperature. The measurement system consisted of a lock-in amplifier (SR850), a bipolar amplifier (BA4825), a DC amplifier (BOP 36-12ML), a DC electromagnet, and a Helmholtz coil. Voltage changes in response to the sinusoidal AC magnetic field of 10^{-4} T at 1 kHz generated by the Helmholtz coil was recorded at every 0.1 sec during an AC magnetic field sweeping for two successive cycles with a constant field loading/unloading rate.

Structural Analysis of Compositionally-Modified PFN Systems: X-ray diffraction (XRD, D/MAX2500V/PC) with Cu-Kα radiation was used for the structural analysis for a 2θ range of 20°–80° with a step size of 0.02°. The soft X-ray absorption spectra at both the Ni and Fe *L* edges were measured at the BL25SU beamline in SPring-8. The total electron yield method was used with 96% circularly polarized incident X-rays under an applied magnetic field of 1.9 T. The incident light direction was inclined by 10° with respect to the magnetic field direction. The XMCD spectrum is given by the difference of the two spectra; $\Delta I = I_+ - I_-$ where I_+ and I_- are the intensities when the incident photon direction and the magnetization vectors are parallel and antiparallel, respectively. A detailed experimental description of the setup for the soft XMCD measurements can be found elsewhere.[54] Neutron diffraction data were collected using the nanoscale-ordered materials diffractometer (NOMAD) instrument at the Spallation Neutron Source at Oak Ridge National Lab. Bragg Rietveld refinements of the four highest-resolution detector banks were performed using TOPASv6. Samples were characterized using X-ray and neutron diffraction (see ESI).

DFT Calculation Method: DFT calculations were employed in the local spin-density approximation (LSDA+ U) scheme as implemented in the software package VASP.5.4.1.[55] It can be claimed that the varying of U in the range of 3–5 eV does not appreciably change the values of the Ni and Fe magnetic moments.[56] Indeed, we found that the tendency of the magnetic interaction between Ni and Fe ions remains the same, from the results of various U and J values. Ni spin prefers to be aligned in parallel rather than antiparallel to the nearest Fe spin (See. Figure S12, Supporting Information). Among them, as one of the simplest cases, U = 5 eV and J = 0 eV were used for Fe^{3+} and Ni^{2+} ions in the Lichtenstein scheme.[57] The projector-augmented wave method was in the VASP potentials for Pb (5d, 6s, and 6p), Ni (3p, 3d, and 4 s), Fe (3p, 3d, and 4 s), Nb (4s, 4p, 4d, and 5 s), and O (2s and 2p). A 3 × 2 × 1 Monkhorst–Pack k-point grid was used for integrations within the Brillouin zone for a cell containing 12 formula units.[58] The space group was R3m with G-type antiferromagnetic ordering. We assumed that Fe and Nb atoms were disordered. The calculated cell contained 12 formula units of PFN with a = 5.5784(3) Å, b = 9.7491(1) Å and c = 13.7628(2) Å. The magnetic moments of the Fe ions were ≈–4.19 μ_B for down spin and 4.16 μ_B for up spin, whereas that of the Ni ions is –1.62 μ_B. The energy cut-off for the plane wave basis was set to 500 eV and the force criteria for the structure optimization was 0.01 eV Å^{-1}. Spin–orbit coupling was included with the bulk G-type antiferromagnetic order to determine the spin-canting and weak ferromagnetic moments by magnetic anisotropy calculation.

Supporting Information

Supporting Information is available from the Wiley Online Library or from the author.

Acknowledgements

J.-H.P. and J.-H.C. contributed equally to this work. This research was supported by the Material Technology Development Program (No. 1415182019) through the Korea Evaluation Institute of Industrial Technology (KEIT). The work at SNU was supported by the NRF through the Quantum Computing Research Infrastructure Construction Program (2022M3K2A1083855) and by the Ministry of Education through the core center Program (2021R1A6C101B418).

Conflict of Interest

The authors declare no conflict of interest.

Data Availability Statement

The data that support the findings of this study are available from the corresponding author upon reasonable request.

Keywords

ferroelectricity/ferroelectric oxides, ferromagnetism/ferromagnetic oxides, magnetoelectric coupling, multiferroics, superexchange interaction

Received: May 9, 2024
Revised: August 30, 2024
Published online:

[1] M. Fiebig, T. Lottermoser, D. Meier, M. Trassin, *Nat. Rev. Mater.* **2016**, *1*, 16046.
[2] J.-M. Hu, C.-W. Nan, *APL Mater.* **2019**, *7*, 080905.
[3] N. A. Spaldin, R. Ramesh, *Nat. Mater.* **2019**, *18*, 203.
[4] J. F. Scott, *Nat. Mater.* **2007**, *6*, 256.
[5] S. Manipatruni, D. E. Nikonov, C. C. Lin, T. A. Gosavi, H. Liu, B. Prasad, Y. L. Huang, E. Bonturim, R. Ramesh, I. A. Young, *Nature* **2019**, *565*, 35.
[6] M. A. Jalaja, S. Dutta, *Adv. Mater. Lett.* **2015**, *6*, 568.
[7] M. Nair, R. Guduru, P. Liang, J. Hong, V. Sagar, S. Khizroev, *Nat. Commun.* **2013**, *4*, 1707.
[8] J.-H. Cho, W. Jo, *J. Korean Inst. Electr. Electron. Mater. Eng.* **2021**, *34*, 149.
[9] J.-H. Cho, W. Jo, *Ceramist* **2021**, *24*, 228.
[10] D. Khomskii, *Physics* **2009**, *2*, 20.
[11] S.-W. Cheong, M. Mostovoy, *Nat. Mater.* **2007**, *6*, 13.
[12] W. Eerenstein, N. D. Mathur, J. F. Scott, *Nature* **2006**, *442*, 759.
[13] C. Lu, M. Wu, L. Lin, J.-M. Liu, *Natl. Sci. Rev.* **2019**, *6*, 653.
[14] J. Wang, J. B. Neaton, H. Zheng, V. Nagarajan, S. B. Ogale, B. Liu, D. Viehland, V. Vaithyanathan, D. G. Schlom, U. V. Waghmare, N. A. Spaldin, K. M. Rabe, M. Wuttig, R. Ramesh, *Science* **2003**, *299*, 1719.
[15] C. Ederer, N. A. Spaldin, *Phys. Rev. B* **2005**, *71*, 060401.
[16] N. A. Hill, *J. Phys. Chem. B* **2000**, *104*, 6694.
[17] A. Sundaresan, N. V. Ter-Oganessian, *J. Appl. Phys.* **2021**, *129*, 060901.
[18] T. Kimura, *Annu. Rev. Condens. Matter Phys.* **2012**, *3*, 93.
[19] Y. Tokura, S. Seki, *Adv. Mater.* **2010**, *22*, 1554.
[20] X. Liu, R. Hong, C. Tian, *J. Mater. Sci.: Mater. Electron* **2008**, *20*, 323.
[21] V. M. Goldschmidt, *Naturwissenschaften* **1926**, *14*, 477.
[22] J.-H. Cho, J.-H. Lee, H. Jang, N. J. Lee, W.-S. Kang, G.-T. Hwang, S. Kim, M. G. Kim, W. Jo, *J. Appl. Phys.* **2021**, *130*, 094101.
[23] N. R. Ko, J. H. Cho, J. M. Jang, W. Jo, *J. Korean Inst. Electr. Electron. Mater. Eng.* **2021**, *34*, 386.
[24] C. Zener, R. R. Heikes, *Rev. Mod. Phys.* **1953**, *25*, 191.
[25] J. B. Goodenough, *J. Solid State Chem.* **1996**, *127*, 126.
[26] J. Kanamori, *J. Phys. Chem. Solids* **1959**, *10*, 87.
[27] M. A. Gilleo, *Phys. Rev.* **1958**, *109*, 777.
[28] J. F. Scott, *NPG Asia Mater* **2013**, *5*, e72.
[29] M. P. Singh, K. D. Truong, S. Jandl, P. Fournier, *J. Appl. Phys.* **2010**, *107*, 09D917.
[30] Y. Yang, J. M. Liu, H. B. Huang, W. Q. Zou, P. Bao, Z. G. Liu, *Phys. Rev. B* **2004**, *70*, 132101.
[31] B. D. Cullity, *Elements of X-Ray Diffraction*, Addison-Wesley Publishing, San Francisco, CA, USA **1956**.
[32] J. Rodriguez-Carvajal, presented at Satellite *Meeting* on *Powder Diffraction* of the XV *Congress* of the IUCr, Toulouse, France, July **1990**, 127.
[33] D. H. Kim, H. J. Lee, G. Kim, Y. S. Koo, J. H. Jung, H. J. Shin, J. Y. Kim, J. S. Kang, *Phys. Rev. B* **2009**, *79*, 033402.
[34] P. Kumari, M. Zzaman, S. Jena, M. Kumar, R. R. Bharadwaj, V. K. Verma, R. Shahid, K. Amemiya, V. R. Singh, *J. Supercond. Nov. Magn.* **2021**, *34*, 1119.
[35] R. J. Mossanek, G. Dominguez-Canizares, A. Gutierrez, M. Abbate, D. Diaz-Fernandez, L. Soriano, *J. Phys. Condens. Matter.* **2013**, *25*, 495506.
[36] K. Kubobuchi, M. Mogi, M. Matsumoto, T. Baba, C. Yogi, C. Sato, T. Yamamoto, T. Mizoguchi, H. Imai, *J. Appl. Phys.* **2016**, *120*, 142125.
[37] V. R. Mastelaro, E. D. Zanotto, *Materials* **2018**, *11*, 204.
[38] R. Sarangi, *Coord. Chem. Rev.* **2013**, *257*, 459.
[39] M. G. Kim, H. S. Cho, C. H. Yo, *J. Phys. Chem. Solids* **1998**, *59*, 1369.
[40] A. Mesquita, B. M. Fraygola, V. R. Mastelaro, J. A. Eiras, *J. Phys. Conf. Ser.* **2013**, *430*, 012111.
[41] J. B. Neaton, C. Ederer, U. V. Waghmare, N. A. Spaldin, K. M. Rabe, *Phys. Rev. B* **2005**, *71*, 014113.
[42] R. O. Kuzian, I. V. Kondakova, A. M. Daré, V. V. Laguta, *Phys. Rev. B* **2014**, *89*, 024402.
[43] H. Xiang, C. Lee, H. J. Koo, X. Gong, M. H. Whangbo, *Dalton Trans.* **2013**, *42*, 823.
[44] S. Chillal, M. Thede, F. J. Litterst, S. N. Gvasaliya, T. A. Shaplygina, S. G. Lushnikov, A. Zheludev, *Phys. Rev. B* **2013**, *87*, 220403.
[45] A. Levstik, V. Bobnar, C. Filipič, J. Holc, M. Kosec, R. Blinc, Z. Trontelj, Z. Jagličić, *Appl. Phys. Lett* **2007**, *91*, 012905.
[46] J. H. Cho, S. Cho, J. H. Lee, H. Palneedi, J. H. Lee, H. P. Kim, N. J. Lee, S. Tigunta, S. Pojprapai, S. Kim, J. Ryu, Y. S. Oh, S. Hong, W. Jo, *J. Am. Ceram. Soc.* **2021**, *104*, 6384.
[47] J.-H. Cho, Y. J. Kim, S. H. Kim, Y.-J. Lee, J.-Y. Choi, G.-T. Hwang, J. Ryu, S. K. Kwak, W. Jo, *J. Am. Ceram. Soc.* **2022**, *105*, 2655.
[48] J. K. Dey, A. Chatterjee, S. Majumdar, A. C. Dippel, O. Gutowski, M. v. Zimmermann, S. Giri, *Phys. Rev. B* **2019**, *99*, 144412.
[49] M. Hoppe, *Magnetic, Structural, and Electronic Properties of $NiFe_2O_4$ Ultrathin Films*, Vol. *118*, Forschungszentrum Jülich GmbH, Jülich, Germany **2016**.
[50] T. Moriya, *Phys. Rev.* **1960**, *120*, 91.
[51] T. Moriya, *Phys. Rev. Lett.* **1960**, *4*, 228.
[52] H. Katsura, N. Nagaosa, A. V. Balatsky, *Phys. Rev. Lett.* **2005**, *95*, 057205.
[53] I. A. Sergienko, E. Dagotto, *Phys. Rev. B* **2006**, *73*, 094434.
[54] T. Nakamura, T. Muro, F. Z. Guo, T. Matsushita, T. Wakita, T. Hirono, Y. Takeuchi, K. Kobayashi, *J. Electron Spectrosc. Relat. Phenomena* **2005**, *144*, 1035.
[55] G. Kresse, J. Furthmüller, *Phys. Rev. B* **1996**, *54*, 11169.
[56] C. Zener, *Phys. Rev.* **1951**, *81*, 440.
[57] A. I. Liechtenstein, V. V. Anisimov, J. Zaanen, *Phys. Rev. B* **1995**, *52*, R5467.
[58] H. J. Monkhorst, J. D. Pack, *Phys. Rev. B* **1976**, *13*, 5188.